



# An adaptive concurrent multiscale method for microstructured elastic solids

Franck J. Vernerey\*, Mirmohammadreza Kabiri

Department of Civil, Environmental and Architectural Engineering, University of Colorado, Boulder, USA

## ARTICLE INFO

### Article history:

Received 22 November 2011

Received in revised form 30 March 2012

Accepted 19 April 2012

Available online 8 May 2012

### Keywords:

Concurrent multiscale method

Microstructured material

Homogenization

Strain localization

## ABSTRACT

The present paper introduces a concurrent adaptive multiscale methodology for elasticity problems in which macroscopic deformation strongly interact with microscopic deformation fields at the scale of the microstructure. This situation occurs in a variety of important situations such as ductile fracture, shear banding and when sharp discontinuities are present in the material domain. Our analysis starts from the idea that numerical simulations must ensure that numerical accuracy is maximum while the error from homogenization is minimum. While the first usually implies that element size must be refined, the second implies that elements may not be smaller than the representative volume elements (RVEs) of the microstructure. To accommodate these two conditions, a finite element method is introduced such that continuum elements can be replaced by explicit RVEs through properly defined macro–micro kinetic conditions reminiscent to those used in classical homogenization. When combined with adaptive refinement, the methodology provides a flexible numerical method in which both continuum and microstructural descriptions can naturally coexist within a single simulation. We show, through various examples that the proposed framework addresses the important issue of reaching the optimal modeling accuracy for a minimal computational cost.

© 2012 Elsevier B.V. All rights reserved.

## 1. Introduction

Understanding how the macroscopic behavior of materials depend on their underlying microstructure has been a classical research issue in materials science but is also becoming a key question in biology and medicine. The link between structure and properties is indeed a central feature of the development of fracture resistant and multifunctional materials [53,47] and holds the key to our understanding of how biological tissues respond, evolve and remodel [49,48,43]. A number of methodologies have been introduced to address this problem, most of which can be gathered under the umbrella of homogenization theory [36,21,17,18,54,29,30]. In this context, macroscopic behavior is cast in terms of a constitutive relation that is derived via appropriate average of the microstructure behavior in a representative volume element (or RVE) [11,52,40,28]. The RVE, commonly defined as the smallest material volume that is statistically representative of the microstructure, therefore holds a central role in homogenization. Indeed, its size must always be significantly smaller than the characteristic length scale of the macroscopic problem for continuum assumptions to be valid. As such, continuum theories are usually not capable of accurately capturing material's behavior in situation where highly heterogeneous deformation fields are observed. In elasticity, this typically occurs in the presence of stress

concentrations due to the presence of sharp corners, inclusions or defects whose sizes are comparable to the material's microstructure. In these cases, continuum theory can predict neither the local stress fluctuations at the material's scale (which usually are key to damage nucleation), nor the possible size effects exhibited by the microstructure (such as those observed in cellular materials [2]). Beyond the elastic range, highly heterogeneous deformation are omnipresent in situations such as in fracture [26], shear banding [20,37], and indentation [24,35]. In an effort to improve the predictability of continuum formulation to small scale problems, a number of extensions have been introduced to capture material's size effects and higher deformation modes [35,32,23]. This included higher order continuum theories such as the theory of Cosserat [8,10,14], the micromorphic theory [44–46], the strain-gradient theory [7,12,13] as well as non-local formulations in which the material response of a material point depends on its neighbors [3–5].

Although the above formulations have significantly improved our understanding of small scale material response [46], they are still based on continuum assumptions that implicitly assume a scale separation between the macroscopic problem and the deformation of the RVE. In fact, when the wave length of a macroscopic deformation field is at the same order as that characteristic size of the microstructure, it can be argued that the global material response becomes less important than its local response. In this case, the local response is affected by the stochasticity of the microstructure and a deterministic continuum framework is no

\* Corresponding author.

E-mail address: [franck.vernerey@colorado.edu](mailto:franck.vernerey@colorado.edu) (F.J. Vernerey).

longer applicable. This raises an important issue in multiscale modeling. On the one hand, the above considerations imply that a small scale material description (including microstructural details) is necessary in problems that display highly heterogeneous macroscopic deformation. On the other hand, such a refined description in macroscale domains often leads to an intractable computational problem. An optimal solution is therefore found in methods that can adequately couple a fine material description in regions of highly localized deformation and a coarse description in regions of homogeneous deformation. This idea was used in concurrent methods such as the bridging scale method [37,31,50,6] in which a microscopic region (near a crack tip for instance) can be determined a priori. Such methods are then able to couple continuum models (such as finite element) and small scale material descriptions (such as molecular dynamics). A recurrent problem, however, is that the small scale region cannot, in general, be determined before hand. In this context, Ghosh et al. [19,16,34,39,38] introduced a concurrent multiscale method using Voronoi cell finite element method (VCFEM), which is based on adaptively refining mesh on three different levels of subdomains with various resolutions. The first level is a conventional displacement based finite element model based on constitutive moduli obtained from homogenization of microstructural parameters. The second level is an intermediate level used for switching between macro and micro description models, with higher computational demand compared to the two other levels. The third level subdomain, where damage evolution initiates and periodic boundary condition assumptions for microstructural RVE fail, a detailed microstructural model is formulated using VCFEM. This method addresses damage evolution in composites and heterogeneous materials in an accurate and efficient way.

In the present work, we introduce a novel adaptive multiscale method whose fundamental basis rests on the minimization of both numerical error and homogenization error. The numerical error typically arises from the fact that numerical approximations (provided by shape functions in finite elements) introduce a difference between computational and exact solutions in continuum mechanics. While this error is known to decrease with element size, excessive element refinement may lead to a situation in which element size becomes comparable to that of the microstructure. In this case, we show that additional refinement can induce significant errors in the continuum approximation of the material response. To address this issue, we introduce a numerical method in which elements, once they reach a critical size, can be replaced by explicit RVEs that coexist with a macroscopic continuum description. Upon combining this method with conventional adaptive refinement techniques, we obtain a computational formulation that possesses two major advantages. First, it maintains a relatively low computational cost since a coarse scale continuum description is used in regions of homogeneous deformation. Second, it provides a refined description of the microstructure in regions of heterogeneous deformation and does not violate the fundamental assumptions of continuum theories. In addition, the method provides a flexible framework, based on only two levels of material description, in which the location and size of the microscopic domain does not need to be predetermined and can eventually evolve with material deformation.

The paper is organized as follows. In the next section (Section 2), we provide an analysis of two different types of errors that may arise in a finite element analysis and derive a criterion that governs the allowable element size. In Section 4 we then introduce a bridging scale method in order to enable RVEs to coexist with a surrounding macroscopic finite element mesh. In the 4th section we combine the embedded RVE method with adaptive refinement in order to derive the final form of the proposed method. A few examples are then discussed to assess the efficiency and accuracy

of the framework. Section 5 finally provides a summary of the work and suggests few improvements and extensions for the future.

## 2. Error in homogenization theory and finite elements

One of the principal objectives of multiscale methods is to ensure that modeling accuracy is maximum while the computational cost is minimum. A low computational cost can usually be obtained by using a coarse-grained homogenized continuum model such that unnecessary “fine scale” degrees of freedom are appropriately smeared out. Such an approach, however can introduce some inaccuracies in the solution, especially when the typical wave length of deformation is on the order of characteristic length of the microstructure. In fact, modeling accuracy might be dictated by several factors. On the one hand, numerical discretization error arises from the fact that the approximation provided by finite elements does not exactly capture the exact continuum fields such as displacement, strains or stresses in most situations. On the other hand, a so-called homogenization error may arise from the fact that continuum theories can only describe an average material response, which may not be enough in certain cases. We see in this section that these two types of errors lead, in certain situations, to very inappropriate solutions if continuum theories are solely used.

### 2.1. Homogenization error

Let us first assess the homogenization error that can result from the use of coarse grain continuum formulations. We base our arguments on classical first-order continuum theories, i.e., the stored energy in an elastic body exclusively depends on the first gradient of the displacement fields. While this may seem restrictive, the arguments presented in this section may be extended to high-order theories if needed.

Consider a macroscopic elastic body that is contained in a closed domain  $\Omega$  and delimited by a boundary  $\Gamma$ . Referring to a Cartesian coordinate system with coordinates  $\{x_i\}$ ,  $i = 1, 2, 3$ , the state of a material point  $P$ , located at position  $\mathbf{x}$  can usually be described in terms of continuum quantities such as the displacement field  $\mathbf{u}(\mathbf{x})$ , the strain field  $\boldsymbol{\epsilon}(\mathbf{x})$  or the stress field  $\boldsymbol{\sigma}(\mathbf{x})$ . From a multiple-scale view point, these macroscopic quantities are interpreted as averages over a material domain that is small relative to macroscopic dimensions. As depicted in Fig. 1, this domain is often denoted as the representative volume element (or RVE) and traditionally defined as the smallest material domain that statistically describes the material's microstructure. For simplicity, we represent such an RVE as a square domain  $\hat{\Omega}$  with side length of  $\hat{L}$ , delimited by a boundary  $\hat{\Gamma}$  and in which the highly fluctuating microscopic displacement, strain and stress fields are represented by  $\hat{\mathbf{u}}$ ,  $\hat{\boldsymbol{\epsilon}}$  and  $\hat{\boldsymbol{\sigma}}$ , respectively. Relationships between macro and micro quantities (represented by  $\diamond$  here) are then established in terms of the average operation:

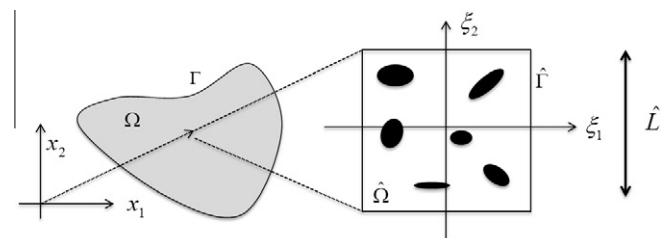


Fig. 1. Continuum macrostructure and heterogeneous microstructure associated with the point located at position  $\mathbf{x}$ .

$$\langle \diamond \rangle = \frac{1}{|\hat{\Omega}|} \int_{\hat{\Omega}} \diamond d\hat{\Omega}. \quad (1)$$

In particular, for a first-order continuum theory and small displacement assumptions, an infinitesimal change in macroscale elastic energy  $\delta W$  is related to its microscopic counterpart through the Hill-Mandel condition [42,25]:

$$\delta W = \langle \hat{\boldsymbol{\sigma}} : \delta \hat{\boldsymbol{\epsilon}} \rangle, \quad (2)$$

where  $\delta \hat{\boldsymbol{\epsilon}} = \{\nabla \delta \hat{\mathbf{u}}\}^s$  and the superscript  $s$  is used to denote the symmetric part of the second-order tensor. Consistent with a first-order theory, we assume that the displacement field in the RVE can be given by the expansion:

$$\hat{\mathbf{u}}(\boldsymbol{\xi}) = \hat{\mathbf{u}}(\mathbf{0}) + \langle \hat{\nabla} \hat{\mathbf{u}} \rangle \cdot \boldsymbol{\xi} + \frac{1}{2} \boldsymbol{\xi} \cdot \langle \hat{\nabla} \hat{\nabla} \hat{\mathbf{u}} \rangle \cdot \boldsymbol{\xi} + \hat{\mathbf{u}}^f(\boldsymbol{\xi}). \quad (3)$$

Here,  $\boldsymbol{\xi}$  is a nondimensional local coordinate defined as  $\boldsymbol{\xi} = (\mathbf{y} - \mathbf{x})/\hat{L}$  and the vector  $\mathbf{y}$  is the position vector in a coordinate system whose origin is the geometric center of the RVE. Furthermore, the local gradient operator is defined as  $\hat{\nabla} = \partial/\partial \boldsymbol{\xi}$  and the quantity  $\hat{\mathbf{u}}^f(\boldsymbol{\xi})$  describes the fluctuating component of the displacement that is not captured by the series expansion. Now realising that the average fields at the microscale are equal to the macroscale fields, we obtain:

$$\langle \hat{\nabla} \hat{\mathbf{u}} \rangle = \hat{L} \nabla \mathbf{u} \quad \text{and} \quad \langle \hat{\nabla} \hat{\nabla} \hat{\mathbf{u}} \rangle = \hat{L}^2 \nabla \nabla \mathbf{u}. \quad (4)$$

Using this approximation in (3) and subsequently in (2) leads to the following expression of the macroscopic elastic energy:

$$\delta W = \boldsymbol{\sigma} : \delta \boldsymbol{\epsilon} + \boldsymbol{\tau} : (\hat{L} \nabla \nabla \delta \mathbf{u}) + \langle \hat{\boldsymbol{\sigma}} : \hat{\nabla} \delta \mathbf{u}^f \rangle, \quad (5)$$

where the macro-stress is logically given by  $\boldsymbol{\sigma} = \langle \hat{\boldsymbol{\sigma}} \rangle$  and the stress-couple  $\boldsymbol{\tau}$  is introduced as  $\boldsymbol{\tau} = \langle \hat{\boldsymbol{\sigma}} \otimes \boldsymbol{\xi} \rangle$ . Since first-order theories only express the elastic energy in terms of the first term on the right hand-side, it remains valid only if the last two terms are sufficiently small to be neglected. As will be discussed in Section 3.1.2, the last term identically vanishes by enforcing proper boundary conditions in the RVE. The middle term, however, can only be neglected if

$$\boldsymbol{\tau} : (\hat{L} \nabla \nabla \delta \mathbf{u}) \ll \boldsymbol{\sigma} : \delta \boldsymbol{\epsilon}. \quad (6)$$

The couple stress  $\boldsymbol{\tau}$  is a bounded quantity [30] that can only remain within the same order of magnitude as the macrostress  $\boldsymbol{\sigma}$ . Furthermore, since the strain is typically on the order of (but less than) unity, the above condition can be rewritten in terms of a conditions on the second displacement gradient as follows:

$$e_h = \hat{L} \|\nabla \nabla \mathbf{u}\| \ll 1, \quad (7)$$

where the  $L_2$  norm of the second displacement gradient is written in indicial notation as  $\|\nabla \nabla \mathbf{u}\| = \sqrt{u_{i,jk} u_{i,jk}}$ . Here, we introduced a homogenization error quantity  $e_h$  that must remain small everywhere in  $\Omega$  for first-order theory to remain valid.

## 2.2. Discretization error

As discussed previously, the discretization error is measured by the difference between the exact continuum solution and the solution provided by the numerical scheme (finite elements in our case). In the present work, we are particularly interested in the error in strain fields (or displacement gradient) in individual elements. In this context, let us consider that the body  $\Omega$  is decomposed in a number of finite elements and define  $\Omega_e$  the physical domain associated with an arbitrary element  $e$ . The discretization error  $e_d$  in this element may then be written in terms of the difference between the exact solution of the displacement gradient  $u_{i,j}$

and that provided by the finite element approximation  $u_{i,j}^h$  as follows [9]:

$$e_d = \left( \int_{\Omega_e} (u_{i,j} - u_{i,j}^h)(u_{i,j} - u_{i,j}^h) d\Omega_e \right)^{1/2}, \quad (8)$$

where the Einstein convention related to summations on repeated indices is applied. To assess this quantity, it is useful to introduce a local Cartesian coordinate system  $z_i$  with origin in the geometric center of the element, in which the exact displacement field can be written in term of a Taylor series expansion as:

$$u_i(\mathbf{z}) = \bar{u}_i + \chi_{ij} z_j + \frac{1}{2} H_{ijk} z_j z_k + O(\mathbf{z}^3), \quad (9)$$

where  $\bar{\mathbf{u}}$  is a displacement vector at  $\mathbf{z} = 0$ ,  $\boldsymbol{\chi}$  is interpreted as the deformation gradient tensor and  $\mathbf{H}$  is a third-order tensor representing the second displacement gradient in the element. Further, for first-order continua, it is sufficient to consider linear (or bi-linear) two-dimensional elements in which the displacement  $\mathbf{u}_h$  can be written as a function of  $\mathbf{z}$  as:

$$u_i^h(\mathbf{x}) = \bar{u}_i^h + \chi_{ij}^h z_j. \quad (10)$$

Here, the superscript  $h$  denotes the numerical solution. Note that for four nodes finite element, the approximate displacement also contains some bi-linear terms, but this does not affect the remainder of the derivations. The difference between exact and approximate displacement therefore reads:

$$u_i(\mathbf{z}) - u_i^h(\mathbf{z}) = e_i + B_{ij} z_j + \frac{1}{2} H_{ijk} z_j z_k, \quad (11)$$

where  $\mathbf{e} = \bar{\mathbf{u}} - \bar{\mathbf{u}}^h$  and  $\mathbf{B} = \boldsymbol{\chi} - \boldsymbol{\chi}^h$ . The above equation is representative of a family of conics with center  $\mathbf{z}_c$  [9]. Furthermore, it can be shown that the error in displacement shown in (11) identically vanishes at nodal locations and takes a maximum value at the center  $\mathbf{z}_c$  of the cone. One can further find that [9], under an appropriate change of coordinate, (11) can be rewritten in terms of the error  $\varepsilon$  at the center of the cone and new coordinates  $\bar{\mathbf{z}}$  that have their origin at  $\mathbf{z}_c$ , in the form:

$$u_i(\mathbf{z}) - u_i^h(\mathbf{z}) = \varepsilon_i - \frac{1}{2} H_{ijk} \bar{z}_j \bar{z}_k. \quad (12)$$

For the sake of simplicity, let us evaluate the error in a square element, whose size  $h$  is given by the length of its side. In this case, the center of the cone coincides with the geometric center of the element, i.e.,  $\mathbf{z} = \bar{\mathbf{z}}$ . Substituting (12) in (8) then leads to:

$$e_d^2 = H_{ijm} H_{ijn} \int_{\Omega_e} z_m z_n d\Omega = \frac{h^2}{12} H_{ijk} H_{ijk}. \quad (13)$$

Recognizing that the tensor  $\mathbf{H}$  is a measure of the second displacement gradient  $\nabla \nabla \mathbf{u}$  in the element, the discretization error can finally be written as:

$$e_d = hc \|\nabla \nabla \mathbf{u}\|, \quad (14)$$

where  $c = 1/\sqrt{12}$  and the  $L_2$  norm  $\|\cdot\|$  was defined in the previous section. This result shows, as discussed in [51], that the discretization error can be written in terms of the second displacement gradient and is a decreasing function of the element size  $h$ . This is a particularly useful result as the evolution of both discretization and homogenization errors may now be assessed in terms of element size. For instance, let us consider a situation in which the norm of the second displacement gradient  $\|\nabla \nabla \mathbf{u}\|$  is fixed and we wish to investigate the gain in accuracy by decreasing the element size  $h$ . Using (7) and (14), it is possible to plot both homogenization and discretization errors as a function of  $h$  as illustrated in Fig. 2a. By defining the total error  $e$  as the maximum of  $e_h$  and  $e_d$ , it becomes clear that the error decreases linearly with element size as

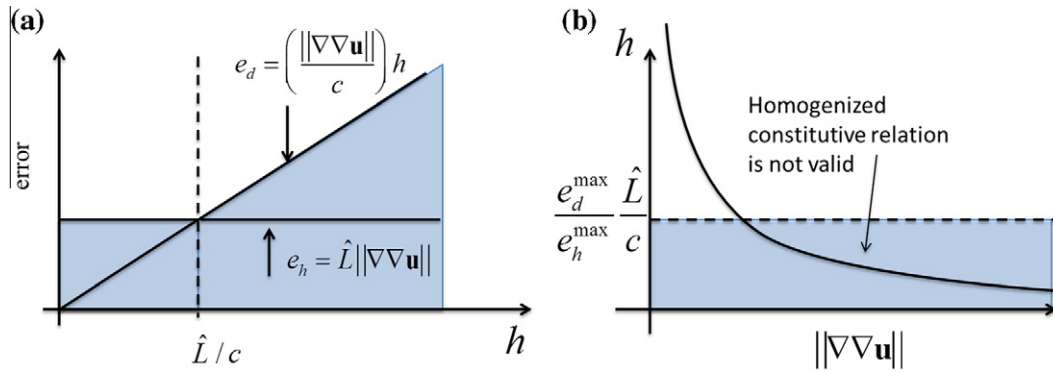


**Fig. 2.** (a) Evolution of error measures with element size when the quantity  $\|\nabla\nabla\mathbf{u}\|$  is fixed. (b) Critical element size in terms of the norm of the second displacement gradient  $\|\nabla\nabla\mathbf{u}\|$ .

long as  $h > \hat{L}/c$ . However, further refinement ( $h < \hat{L}/c$ ) ceases to improve the accuracy of the solution as the homogenization error becomes dominant.

2.3. Limits of the continuum based finite element method

From the above analysis, it can be seen that, in order to be accurate, a solution must ensure that both the homogenization error  $e_h$  and the discretization error  $e_d$  are significantly smaller than unity. Practically, we can therefore define maximum allowable errors  $e_h^{\max}$  and  $e_d^{\max}$  such that the solution is satisfactory if:

$$e_h < e_h^{\max} \quad \text{and} \quad e_d < e_d^{\max}. \tag{15}$$

We note here that the quantity  $e_h^{\max}$  measures the difference between the typical length scale associated with strain gradient and the size of RVEs. To ensure that we do not violate the assumptions of continuum mechanics, a guideline would consist of choosing  $e_h^{\max}$  such that  $\|\nabla\nabla\mathbf{u}\|$  remains smaller than 1% of  $1/\hat{L}$ , i.e.  $e_h^{\max}$  is less than 0.01. In contrast, the discretization error measures the difference between the finite element approximation and the analytical solution. The choice of  $e_d^{\max}$  is therefore an important indicator of numerical accuracy. In the present study, we choose  $e_d^{\max} = 0.01$ , i.e. the numerical solution is always at least 99% accurate. Since the discretization error decreases with element size, according to (14), classical refinement techniques can be used such that the size of elements is smaller than a critical size  $h^c$  defined as:

$$h^c = \frac{e_d^{\max}}{c\|\nabla\nabla\mathbf{u}\|}. \tag{16}$$

As a result, it can be seen that as the second gradient of deformation increases, the element size should inversely decrease in the fashion exhibited in Fig. 2b. Now enforcing the condition on homogenization error in the form  $\hat{L}\|\nabla\nabla\mathbf{u}\| < e_h^{\max}$  and using (16), one obtains the following condition on the element size  $h^c$ :

$$h^c > \frac{e_d^{\max}}{c(e_h^{\max})} \hat{L}. \tag{17}$$

This enforces a strong condition on the critical element size so that the assumptions of first-order continuum theory are satisfied. As depicted in Fig. 2b, an element's size reaches a critical value  $h^c = \hat{L}(e_d^{\max}/c(e_h^{\max}))$  when the second displacement gradient is such that  $\|\nabla\nabla\mathbf{u}\| = e_h^{\max}/\hat{L}$ . This result is important as it implies that in certain cases, the variation of strain is so large that the validity of the continuum theory fails regardless of the size of elements. To better understand this, let us consider the case in which the relation between the maximum discretization and homogenization errors is  $e_d^{\max} = c(e_h^{\max})$ . In this case, (17) states that continuum assumptions are violated if the element size is smaller than the size  $\hat{L}$  of the RVE. One can interpret this as follows. When the element size is larger than that of the RVE, they can be considered as appropriate domains on which homogenized material response can be used. However, as they become smaller than the RVE, the average material response is no longer valid and elements should be replaced by a more accurate description of the material's structure. To address this issue, we next introduce a computational method that naturally substitutes continuum elements by RVE when the minimum element size is such that it violates homogenization theory. The method guarantees that both discretization and homogenization errors converge to small values, regardless of the second displacement gradients.

3. Finite element with embedded RVE

As discussed above, when the size of elements becomes close to that of the RVEs, the validity of homogenized constitutive relation breaks down. Relying on the error criterion deduced above, we derive a numerical approach in which finite elements can be replaced by RVEs in the case when element size becomes critical ( $h = h_c$ ). This idea is depicted in Fig. 3, in which the cases of a single embedded RVE and a patch of embedded RVEs are shown. A potential

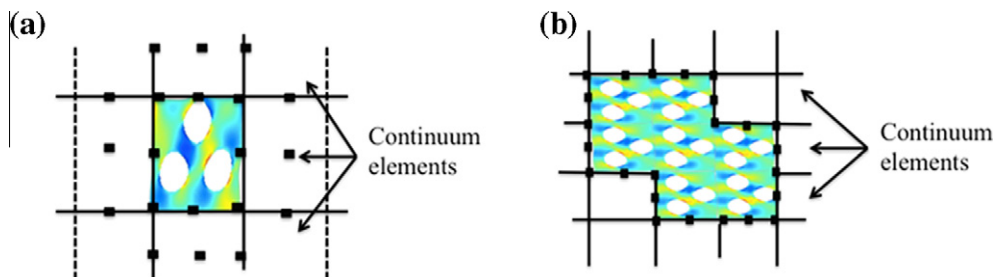


**Fig. 3.** Illustration of embedded RVE in a macroscopic finite element mesh; (a) case of a single embedded RVE and (b) case of a patch of embedded RVEs.

issue with this method is that RVEs and macroscale elements are representative of a material at very different resolutions and the bridging between macroscopic forces and displacements and their microscopic counterparts is usually subjected to debates. This section addresses this issue by introducing three possible types of macro–micro conditions.

### 3.1. Multiscale RVE-FEM bridging method

To appropriately bridge the mechanics of an embedded RVE to the surrounding macroscopic elements, it is first useful to derive a relationship between the kinematics at the macroscopic (continuum element) and microscopic (RVE) level. This is the object of this subsection.

#### 3.1.1. Macro–micro kinematic

Let us consider an initially rectangular shaped RVE on which a macroscopic finite element is superposed (Fig. 3a). The kinematic compatibility conditions then imposes that the deformation of the element is “in average” the same as that of the RVE. To investigate the mathematical consequence of such a statement, let us first write the microscopic displacement in the RVE as follows:

$$\mathbf{u}(\xi) = \sum_I N^I(\xi) \mathbf{U}^I + \mathbf{u}^f(\xi), \quad (18)$$

where  $N^I$  is the macroscale shape function associated with node  $I$  and  $\mathbf{u}^f(\xi)$  is an arbitrary fluctuation field. The displacement gradient in the element may then be written in terms of the differential operator  $\hat{\nabla}$  as:

$$\hat{\nabla} \mathbf{u}(\xi) = \sum_I \mathbf{B}^I(\xi) \mathbf{U}^I + \hat{\nabla} \mathbf{u}^f(\xi), \quad (19)$$

where we introduced the derivatives of shape functions as  $\mathbf{B}^I = \partial N^I / \partial \xi$ . The average displacement gradient in the RVE can then be written as:

$$\langle \hat{\nabla} \mathbf{u} \rangle = \sum_I \langle \mathbf{B}^I \rangle \mathbf{U}^I + \langle \hat{\nabla} \mathbf{u}^f \rangle, \quad (20)$$

where the average deformation of the element is given by the first term on the right hand side. Thus, the compatibility of RVE and element deformation implies that the gradient of fluctuation fields must vanish, in average, in the RVE. This yields:

$$\langle \hat{\nabla} \mathbf{u}^f \rangle = \frac{1}{|\hat{\Omega}|} \int_{\hat{\Gamma}} \hat{\mathbf{u}} \otimes \mathbf{n} d\hat{\Omega} = 0, \quad (21)$$

where  $\mathbf{n}$  is the unit normal vector to the boundary of the RVE and we applied the divergence theorem to obtain the surface integral. The above equation is important as it gives a condition on the fluctuating displacement on the edge of the RVE; it will prove useful in deriving coupling conditions between macroscale and microscale as discussed in the next sections.

#### 3.1.2. Relationship between macroscopic and microscopic forces

Let us now assess the relationship between macroscopic nodal forces and microscopic RVE surface forces. In this context, it is useful to first write the variation of energy in an RVE as:

$$\delta \hat{w} = \int_{\hat{\Omega}} \hat{\boldsymbol{\sigma}} : \delta \hat{\boldsymbol{\epsilon}} d\hat{\Omega} = \int_{\hat{\Gamma}} \hat{\mathbf{t}} \cdot \delta \hat{\mathbf{u}} d\hat{\Gamma}, \quad (22)$$

where  $\hat{\mathbf{t}}$  is the Cauchy stress vector on the RVE boundary. Assuming that the variation of energy, associated with the fluctuation field, vanishes globally [29], i.e.,

$$\int_{\hat{\Gamma}} \hat{\mathbf{t}} \cdot \delta \mathbf{u}^f d\hat{\Gamma} = 0, \quad (23)$$

one can substitute (18) in (22) and find the traditional expression for the energy of a macroscopic element:

$$\delta \hat{w} = \sum_I \mathbf{f}^I \cdot \delta \mathbf{U}^I, \quad (24)$$

where the macroscopic nodal forces are related to the traction forces  $\hat{\mathbf{t}}$  on the boundary by:

$$\mathbf{f}^I = \sum_I \int_{\hat{\Gamma}} N^I \hat{\mathbf{t}} d\hat{\Gamma}. \quad (25)$$

It should be noted that the magnitude and distribution of  $\hat{\mathbf{t}}$  depends on the type of displacement fluctuations on  $\hat{\Gamma}$ . We next review three type of conditions on fluctuation fields that find their analogue in traditional computational homogenization.

### 3.2. Types of macro–micro coupling assumptions

#### 3.2.1. Strong displacement coupling

The simplest way of verifying (21) consists of enforcing the fluctuation fields  $\hat{\mathbf{u}}$  to identically vanish at every point on the RVE boundary. Setting  $\hat{\mathbf{u}} = 0$  in (18) yields the following relationship between micro and macro displacement:

$$\mathbf{u}(\xi) = \sum_I N^I(\xi) \mathbf{U}^I, \quad \xi \in \hat{\Gamma}. \quad (26)$$

This condition clearly enforces the microscopic displacement to precisely follow the macroscopic displacement variation interpolated by the macroscopic shape functions. From a numerical view point, the above constraints can typically be enforced with the Lagrange multiplier method, in which two constraints (represented by a vector  $\mathbf{c}$ ) are enforced at every microscopic node that belongs to the boundary. This therefore leads to a system of equations of  $2N^m$  where  $N^m$  is the number of microscopic nodes on the boundary. More precisely, considering a microscopic node  $n$  on  $\hat{\Gamma}$ , the constraint  $\mathbf{c}_n$  is given by:

$$\mathbf{c}_n = \mathbf{u}_n - \sum_I N^I(\xi_n) \mathbf{U}^I = 0, \quad (27)$$

where  $\xi_n$  is the location of node  $n$  in the local coordinate system of the RVE. This constraint is associated with a Lagrange multiplier  $\lambda_n$  that can be identified as the microscopic traction force at node  $n$ . Fig. 4a illustrates the deformation of adjacent microscopic RVE and macroscopic element resulting from a strong displacement coupling. Note that no small scale fluctuations are allowed on the edge of the RVE; this coupling may thus be compared to Dirichlet-type boundary conditions in classical homogenisation, which are known to overestimate the stiffness of the RVE.

#### 3.2.2. Weak displacement coupling

A way to remove some of the constraints on the RVE is to apply the so-called weak displacement coupling. In this case, we seek to minimize the effect of fluctuating fields on each boundary of the RVE. Denoting each of the four boundaries by the parameter  $\alpha$  ( $\alpha = T, B, R, L$  for the top, bottom, right and left boundaries, respectively), an error measure can be defined for each boundary as:

$$e = \int_{\hat{\Gamma}_\alpha} \left( \mathbf{u}(\xi) - \sum_I N^I(\xi) \mathbf{U}^I \right) d\hat{\Gamma} \quad \alpha = T, B, R, L. \quad (28)$$

To enforce that (21) is weakly satisfied, we minimize the error of each boundary with respect to the macroscopic displacements. This leads to the following system:

$$\mathbf{g}^I(\mathbf{U}^J, \mathbf{u}^k) = \frac{\partial e}{\partial \mathbf{U}^I} = 0 \quad \forall I, J \in \hat{\Gamma}, \quad (29)$$

where  $\mathbf{u}^k$  is the displacement of microscopic node  $k$  that belongs to the boundary. It can therefore be noticed that the weak coupling leads to the application of  $2N$  equations, where  $N$  is the number of macroscopic nodes on boundaries  $\hat{\Gamma}_\alpha$  ( $N = 3$  in the illustration

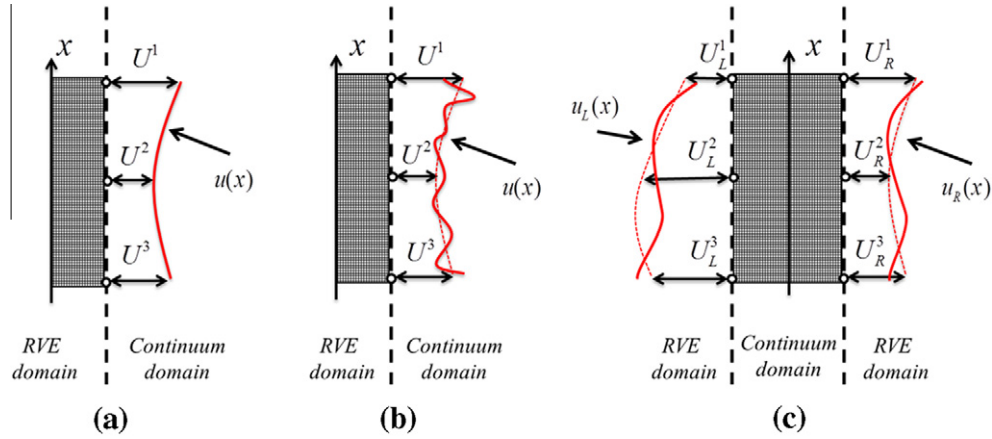


**Fig. 4.** Representation of the three types of micro–macro boundary coupling constraints; (a) strong displacement coupling, (b) weak displacement coupling and (c) quasi-periodic boundary coupling.

in Fig. 4b). Enforcing those constraints via the Lagrange multiplier method leads to the definition of  $2N$  multipliers  $\lambda^l$ , which can be interpreted as macroscopic nodal forces. This usually represents a significant decrease in the number of constraints compared to the strong displacement coupling conditions. Consequences of the weak conditions are depicted in Fig. 4b, in which the microscopic deformation displays fluctuations on the RVE edge although the RVE conform to the deformation of surrounding elements in an average fashion. This situation may thus be thought as analogue to the case of Neumann boundary conditions in classical homogenization.

### 3.2.3. Quasi-periodic boundary coupling

This condition is based upon the assumption of the periodicity of the microstructure and aims to dictate a periodic deformation of RVE while conforming to the surrounding macroscopic continuum. In the case of an initially rectangular RVE considered in this study, it is possible to define two corresponding points on opposite boundaries denoted by  $\hat{\Gamma}_T$  and  $\hat{\Gamma}_B$  for top and bottom RVE boundaries and  $\hat{\Gamma}_L$  and  $\hat{\Gamma}_R$  for left and right boundaries, respectively. Further introducing the outward unit normal vectors to these boundaries by  $\mathbf{n}_T, \mathbf{n}_B, \mathbf{n}_L$  and  $\mathbf{n}_R$ , one can show that (21) is verified if:

$$\tilde{\mathbf{u}}_B(\xi) = \tilde{\mathbf{u}}_T(\xi) \quad \text{and} \quad \tilde{\mathbf{u}}_R(\eta) = \tilde{\mathbf{u}}_L(\eta), \quad (30)$$

where  $\xi$  and  $\eta$  are the local RVE coordinates shown in Fig. 1. This automatically implies from (18) that:

$$\delta \mathbf{u}_T(\xi) - \delta \mathbf{u}_B(\xi) = \sum_I N^I(\xi, 1) \delta \mathbf{U}_T^I - \sum_I N^I(\xi, -1) \delta \mathbf{U}_B^I, \quad (31)$$

$$\delta \mathbf{u}_R(\eta) - \delta \mathbf{u}_L(\eta) = \sum_I N^I(1, \eta) \delta \mathbf{U}_R^I - \sum_I N^I(-1, \eta) \delta \mathbf{U}_L^I. \quad (32)$$

Enforcing these constraints leads to the introduction of Lagrange multipliers for each pair of nodes on corresponding boundaries. These multipliers have the physical meaning of traction forces and can be used to find the macroscopic forces via (25). This type of periodic boundary coupling not only preserves micro structural periodic behavior, which is expected for all periodic materials, but also results in a more physically sound solution compared to other conditions. Using linear quadrilateral elements for continuum modeling of structure, this formulation by itself leads to both periodicity in deformed state and conformity of macro–micro displacement. However, for higher order elements (i.e., quadratic elements), this formulation does not fully ensure conformity of deformation between RVE and macro-elements. To resolve this issue, periodic boundary coupling conditions can be enforced in combination with weak displacement coupling condition on one of two opposite

boundaries ( $\hat{\Gamma}_T$  and  $\hat{\Gamma}_R$ , for instance). As depicted schematically in Fig. 4c, such coupling conditions lead to quasi-periodic deformed state, which allows fluctuation of micro displacement and conformity between RVE and adjacent elements. Note that when large strain and rotation gradient exits, RVEs lose their rectangular shapes and become non-periodic. This is the reason why the term “quasi”-periodic conditions is used. Finally, it is important to mention that since adjacent RVEs share the same microscopic nodes, no Lagrange multipliers are needed for coupling their displacement. The Lagrange multipliers are only used to enforce kinematic constraints between microscopic and macroscopic nodes on the continuum-microstructural boundary.

## 4. Adaptive multiscale method: computational aspects and examples

This section now introduces a multiple scale algorithm that combines the concepts of embedded RVEs discussed above and that of adaptive element refinement. Given a specific elasticity problem, the methodology’s objective is to minimize discretization error via refinement, and to provide maximum accuracy in terms of material modeling by embedding RVEs when the critical element size is reached. The method is based on the algorithm presented in Fig. 5. The numerical method is based on rectangular quadratic (nine-node) finite elements in order to facilitate the calculation of the discretization error defined in (14). In particular, the second gradient of a displacement field in point  $\mathbf{x}$  in a quadratic element can be written as a  $6 \times 1$  matrix as:

$$\nabla \nabla \mathbf{u}(\mathbf{x}) = \begin{bmatrix} \frac{\partial^2 u_x}{\partial x^2} & \frac{\partial^2 u_x}{\partial x \partial y} & \frac{\partial^2 u_x}{\partial y^2} & \frac{\partial^2 u_y}{\partial x^2} & \frac{\partial^2 u_y}{\partial x \partial y} & \frac{\partial^2 u_y}{\partial y^2} \end{bmatrix}^T = \sum_{I=1}^9 \mathbf{G}^I(\mathbf{x}) \mathbf{u}^I, \quad (33)$$

where  $\mathbf{u}^I = [u_x^I, u_y^I]^T$  is nodal displacement vectors at node  $I$  and  $\mathbf{G}^I(\mathbf{x})$  is a matrix given by:

$$\mathbf{G}^I(\mathbf{x}) = \begin{bmatrix} \frac{\partial^2 N_I(\mathbf{x})}{\partial x^2} & \frac{\partial^2 N_I(\mathbf{x})}{\partial x \partial y} & \frac{\partial^2 N_I(\mathbf{x})}{\partial y^2} & 0 & 0 & 0 \\ 0 & 0 & 0 & \frac{\partial^2 N_I(\mathbf{x})}{\partial x^2} & \frac{\partial^2 N_I(\mathbf{x})}{\partial x \partial y} & \frac{\partial^2 N_I(\mathbf{x})}{\partial y^2} \end{bmatrix}^T. \quad (34)$$

With this notation, it is straightforward to show that the L2 norm of second gradient of displacement in a quadratic element takes the form:

$$\|\nabla \nabla \mathbf{u}(\mathbf{x})\|_2 = \left( \sum_{I=1}^9 (\mathbf{u}^I(\mathbf{x}))^T \left( \int_{\Omega} (\mathbf{G}^I(\mathbf{x}))^T \mathbf{G}^I(\mathbf{x}) d\Omega \right) \mathbf{u}^I(\mathbf{x}) \right)^{1/2}. \quad (35)$$

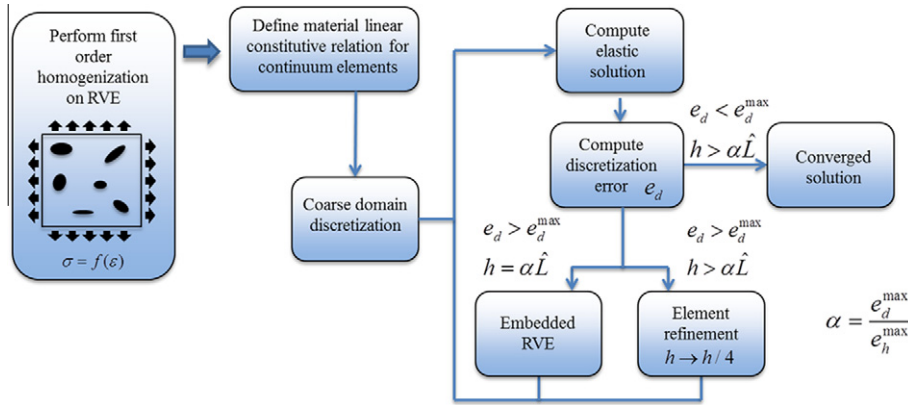


Fig. 5. Algorithm used in the adaptive multiscale method.

Finite element refinement then consists of subdividing elements that display large error measures into four sub-elements. This technique is known to introduce hanging nodes that are present in small elements but are non-existent in adjacent elements of larger size (Fig. 6). To solve this discrepancy, large elements, such as that depicted on the right of Fig. 6, are enriched with addition shape functions associated with the hanging node in a way that conventional conditions on shape functions (continuity and partition of unity) are satisfied. The form of the new shape function, presented in the appendix, ensures that a force equilibrium is appropriately enforced between elements of different sizes.

Upon convergence of the multiscale algorithm, the computational problem reduces, for a linear elastic material undergoing small deformation, into a linear system of the form:

$$\begin{bmatrix} \mathbf{K}_M & \mathbf{0} & \mathbf{I}_{Mm}^T \\ \mathbf{0} & \mathbf{K}_m & \mathbf{I}_{mM}^T \\ \mathbf{I}_{Mm} & \mathbf{I}_{mM} & \mathbf{0} \end{bmatrix} \begin{bmatrix} \mathbf{u}^M \\ \mathbf{u}^m \\ \lambda \end{bmatrix} = \begin{bmatrix} \mathbf{f}^M \\ \mathbf{f}^m \\ \mathbf{c} \end{bmatrix}, \quad (36)$$

where subscript  $M$  and  $m$  represent “macro” continuum elements and the “micro” embedded RVEs, respectively, while  $\mathbf{K}, \mathbf{u}$  and  $\mathbf{f}$  are used to represent stiffness matrices, nodal displacement vector and external force vector, respectively. In addition, the symbol  $\lambda$

represents Lagrange multipliers that enforce the macro–micro conditions  $\mathbf{c} = \mathbf{0}$  derived in the Section 3.2. We note that the stiffness matrix is decomposed into different parts: the first diagonal block  $\mathbf{K}_M$  represents the macroscopic stiffness associated with continuum elements and the second diagonal block  $\mathbf{K}_m$  represents the stiffness arising from the presence of RVEs. Displacements at macro and micro levels are then coupled via the presence of interaction matrices  $\mathbf{I}_{Mm}$  and  $\mathbf{I}_{mM}$  that represent the derivative of the macro–micro constraints  $\mathbf{c}$  with respect to macro and micro displacements, respectively. It can generally be observed that the system is clearly decoupled into a macroscopic problem (continuum elements), a microscopic problem (RVE) and their interactions. Finally, we note that for consistency between micro and macroscales, the constitutive relation at the continuum scale is ultimately derived from a first order computational homogenization procedure (Fig. 5). For instance, in the present study, an isotropic, linear elastic constitutive relation is obtained by relating the average RVE strain to the average RVE stress after subjecting the RVE domain to appropriate boundary conditions. For more information on this method, the reader is referred to [44]. We next illustrate the features of the method and assess its performance in terms of accuracy and cost by considering a few examples. We mostly concentrate on macroscopic elasticity problems for which the material is described at the microscale by a voided linear elastic microstructure. The distribution of voids in the RVE is chosen such that the overall response remains isotropic.

#### 4.1. Example 1: Effect of coupling constraints

The first example aims at investigating the role of using different constraints on the deformation of embedded RVEs. As such, we consider a purely academic problem of a square domain, discretized with eight microscopic elements that possesses an embedded RVE in its center. The domain is then subjected to inhomogeneous deformation through the application of displacement boundary conditions depicted in Fig. 7. The deformation of the embedded RVE is then assessed for the three types of boundary coupling conditions introduced in the previous section.

Regardless of the coupling conditions, it can be seen that the RVE globally displays significant bending modes. This implies that the norm of the second displacement gradients  $\|\nabla\nabla\mathbf{u}\|$  is not negligible and first-order theory cannot accurately describe the mechanical response of the composite. In addition, we note that the type of constraints have a strong effect on the fluctuating strain fields in the RVE. Strong displacement coupling tends to attenuate strain concentrations near the RVE boundary while the weak displacement coupling allow very large fluctuations. The term “quasi-periodic boundary coupling” is also justified in this example,

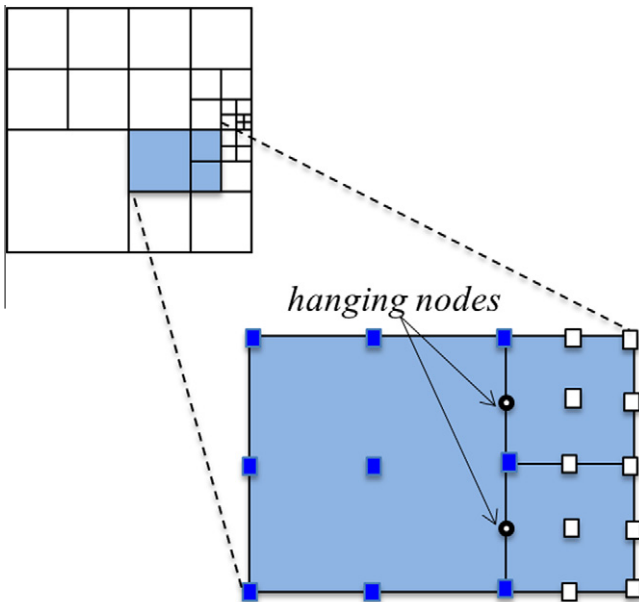
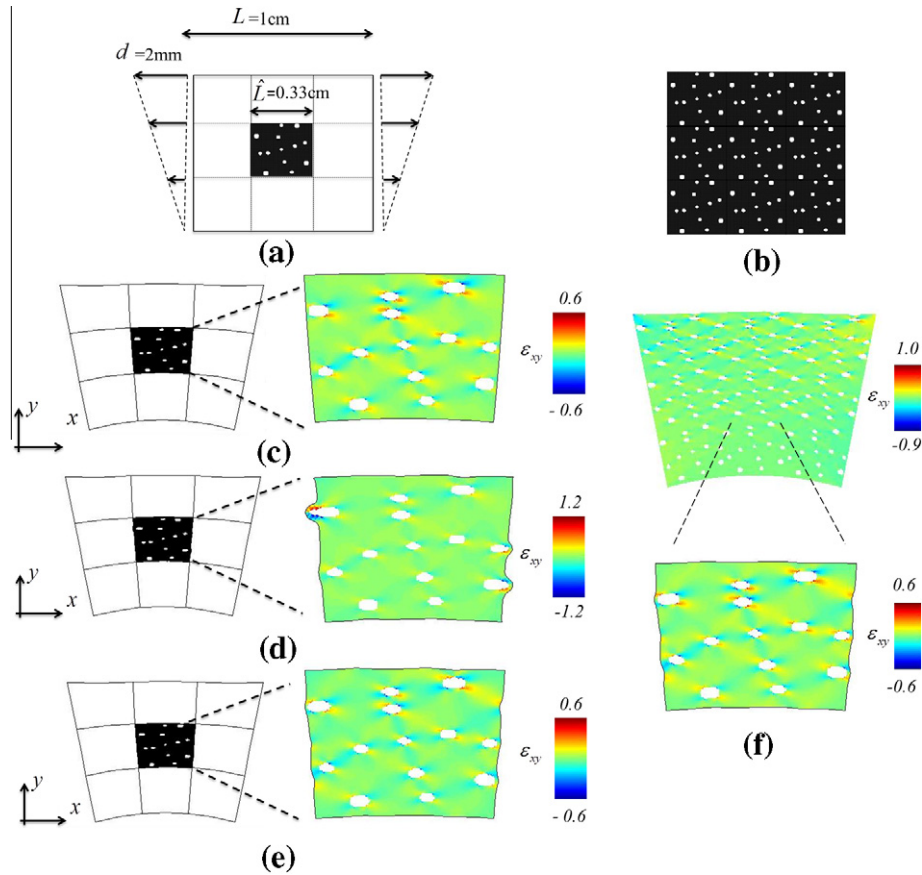


Fig. 6. Illustration of hanging nodes between elements of different sizes.



**Fig. 7.** (a) Single RVE embedded in a continuum region, (b) brute force approach, (c) strong displacement coupling, (d) weak displacement coupling, (e) quasi-periodic boundary coupling and (f) shear strain field obtained from brute force approach.

as seen in Fig. 7, the microscopic displacement fields are periodic across the RVE, while the global RVE deformation is not. We note that the latter constraint provides a better estimation of micro-deformation, as it implicitly assumes that the adjacent macroscopic elements possess a microstructure with the same arrangement as that in the RVE. Furthermore, it is well known from traditional computational homogenization that periodic boundary conditions gives the best estimation of the material behavior. We therefore choose this type of coupling in the next examples. For further validation, we compared the strain fields obtained from these three constraints with numerical results obtained from a “brute force” approach that consists of using a microstructural description in the entire macroscopic domain. This strategy is expected to be highly accurate but its computational cost is often relatively high, if not intractable, for large problems. As shown in Fig. 7f, the strain and deformation fields obtained from the brute force approach are in best agreement with results obtained after applying the quasi-periodic boundary coupling on the embedded RVE.

**4.2. Example 2: Three-point bending test of a porous elastic beam**

The next example illustrates how the combination of finite element adaptivity and the concept of embedded RVE provides an efficient and accurate method to describe problems that are sensitive to multiple length scales. We thus consider a rectangular beam, in plane stress conditions, of length  $L$  and thickness  $L/3$  subjected to three-point bending conditions. More precisely, the beam is supported by two rigid supports of finite-length and subjected to a distributed vertical load  $p$  on its top (Fig. 8). At the microscopic

level, the beam is then represented by a porous linear elastic microstructure represented by the RVE depicted on the right of Fig. 8, for which the matrix is made of rubber with Young’s modulus  $E = 10$  MPa and Poisson’s ratio  $\nu = 0.3$ . continuum elements is obtained from first order computational homogenization. For this material, under the plane strain condition, the homogenized Young’s modulus and Poisson’s ratio are  $E = 4.71$  MPa and  $\nu = 0.338$ , respectively.

This problem is of particular interest as the existence of fixed supports with sharp angles introduces a singular strain field in their neighborhood. This implies that continuum assumptions (for first-order model) are not valid in a small region surrounding the supports, which motivates the use of the proposed multiscale model. We particularly aim to assess the performance of the multiscale framework by measuring computational accuracy and cost for different ratios of material and macroscopic length-scales. On the one hand, cost is measured by the computational time for a specific simulation on a single CPU computer. On the other hand, accuracy is evaluated by comparing the local strain fields near the fixed supports to those predicted by a brute force approach.

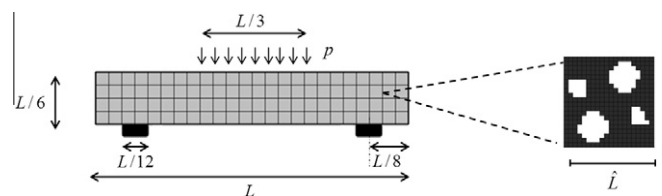


**Fig. 8.** Three point bending test. In this simulation,  $L = 6$  and  $p = 100$  KN/m.

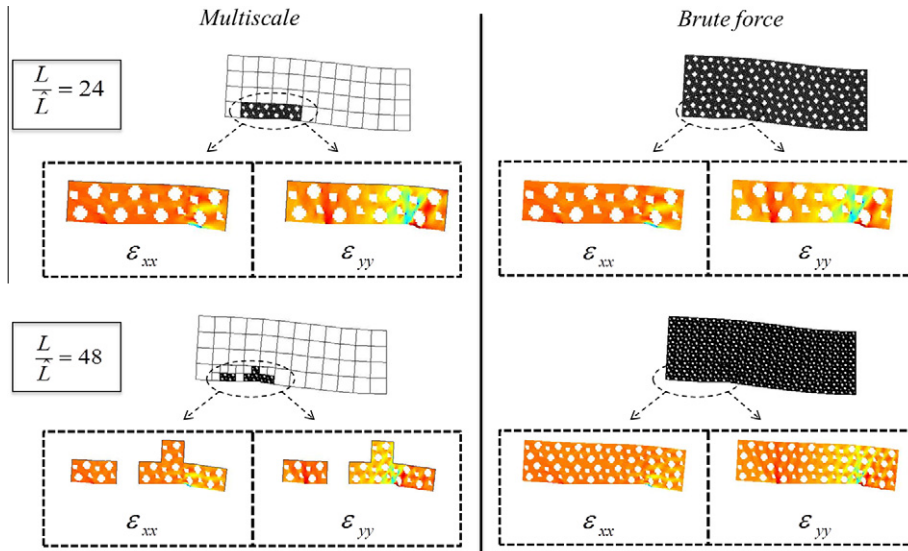


Fig. 9. Results comparison from multiscale (left) and the brute force (right) approaches. Comparisons are provided for  $L/\hat{L} = 24$  (top) and  $L/\hat{L} = 48$  (bottom).

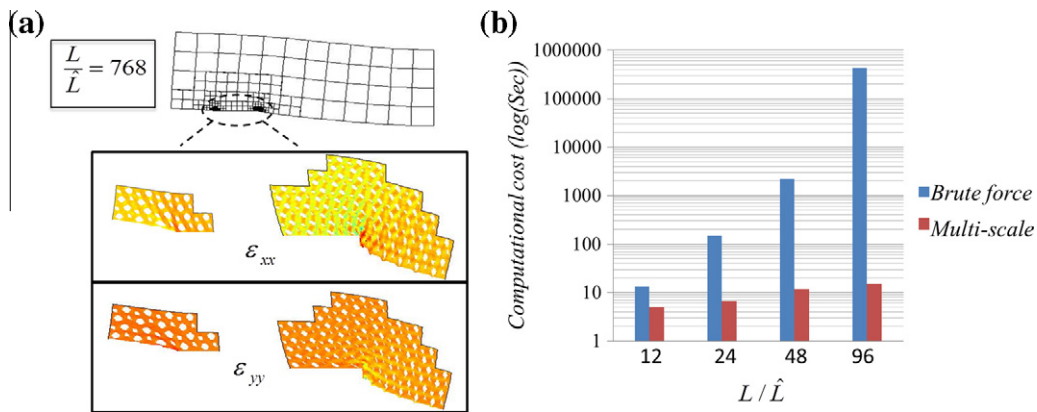


Fig. 10. (a) Beam deflection and microscopic strains in critical regions when  $L/\hat{L} = 768$  in which the very large strain gradient near the support's angles is clearly visible. (b) Computational costs of the brute force and multiscale approaches for different values of  $L/\hat{L}$ .

In this context, Fig. 9 depicts simulation results of the half-beam deflection and the associated microscopic deformation near the support for different situations. In the first case, for a ratio  $\hat{L}/L$  of the RVE size and the beam length equal to 24, as little as two levels of refinements are needed to converge to the final solution. The final solution shows that four RVEs are needed to accurately capture the microstropic strain fields near the supports and the comparison with strain fields computed from a brute force approach are excellent. In the second case, we considered a small microstructure, for which the ratio  $\hat{L}/L$  is 48. Here, three levels of refinement were necessary to reach the final solution which displays seven RVEs split in two regions around the support's two corners. Once again, the local strain prediction from the multiscale method are showing very good agreement with those obtained from the brute force approach. Computational cost comparisons are then given in Fig. 10b for cases in which  $L/\hat{L} = 12, 24, 48$  and 96, respectively. The graph clearly shows that gain in computation time increases drastically as the scale separation between the macroscopic problem and the microstructure becomes more pronounced. This saving is attributed to the fact that the multiscale method only needs an accurate description in critical regions (where large strain gradients exist). As a result, an accurate solution can be obtained for problems that show a very large scale separation such as shown

in Fig. 10a in which  $L/\hat{L} = 768$ . In this case, the corresponding brute simulation was not tractable with a single CPU computer while a converged multiscale solution was obtained after seven stages of refinement.

4.3. Example 3: Stress concentration near a corner

The last example treats another classical elasticity problem that contains a singularity in its solution. Consider the square domain

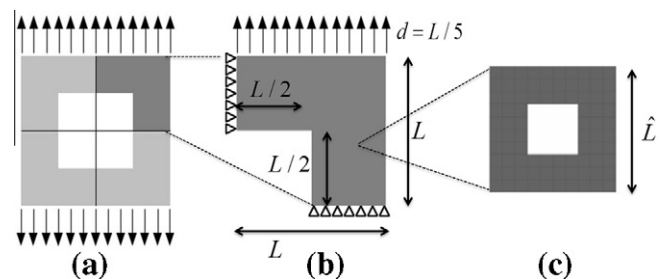


Fig. 11. (a) Original benchmark problem and its reduction using symmetry arguments (b). At the microscale, we consider a periodic microstructure represented by the RVE shown in (c).

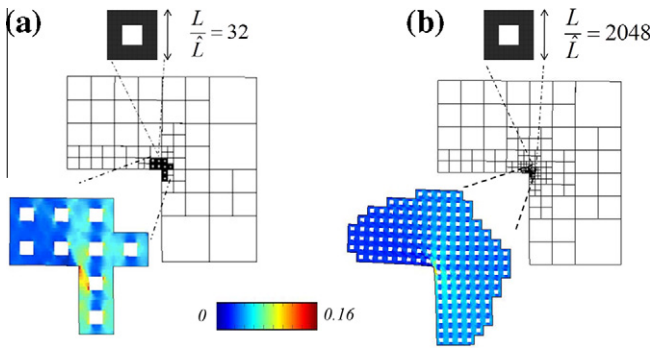


Fig. 12.  $\epsilon_{xx}$  over RVE elements for (a)  $L/\hat{L} = 16$  (b)  $L/\hat{L} = 2048$ .

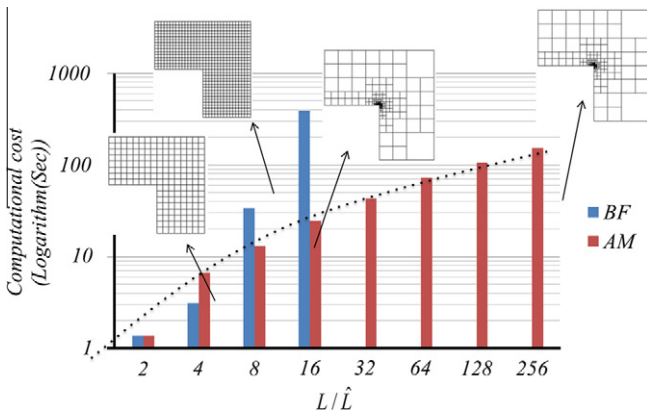


Fig. 13. Comparison between Brute Force approach (BF) and Adaptive Multiscale method (AM) computational cost.

shown in Fig. 11a, subjected to a vertical distributed loading on its top and bottom boundaries. Assume that this solid is represented, at the microscale, by an elastic material that consists of a periodic distribution of small square shaped voids of volume fraction 25%. Material's elastic properties are the same as those used in the previous example. Using symmetry arguments, the domain is then reduced to a quarter of its size (Fig. 11b) with adequate displacement boundary conditions. The presence of a sharp corner induces increasingly large strain gradient as one approaches it; this implies that first continuum theories are limited in providing an accurate solution in this area. In Fig. 12, we present simulation results in the case where the size  $\hat{L}$  of the microstructure is 32 times and 2048 times smaller than the macroscale domain (represented by

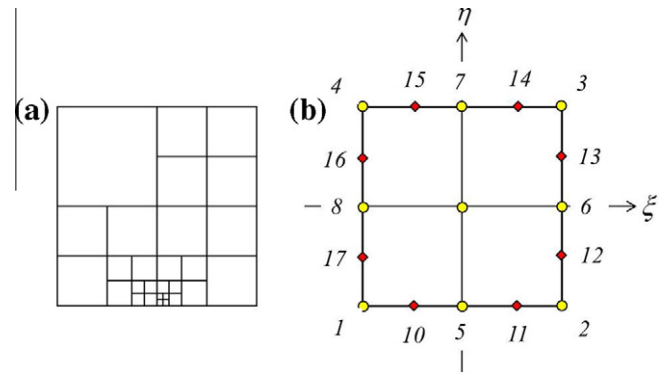


Fig. 15. (a) 1-Irregular mesh, (b) possible hanging nodes positions in an irregular element.

$L$ ), respectively. For both cases, we start from an initial mesh that comprises three square elements of size  $L/2$ . As expected, since the solution exhibits large strain gradients near the corner, adaptive refinement occurs in this region. When the size of element is equal to  $\hat{L}$ , RVEs are naturally embedded in the macroscale, leading to the microscale regions shown in the figure.

Similarly to the previous example, we assessed the efficiency of the method by measuring computational time for different values of  $L/\hat{L}$  ranging from 4 to 256 and compared it to brute force simulations when possible. Once again, the trend showed that brute force simulation time exponentially increases with  $L/\hat{L}$  while the cost of the multiscale simulation remains affordable for very large values of  $L/\hat{L}$ . We also assessed accuracy by computing a local strain value near the corner (see Fig. 13) with both brute force and the multiscale method. As shown in Fig. 14, we obtained an excellent match between the two solutions, confirming that accuracy is maintained despite the lower computational cost.

### 5. Summary and perspectives

In summary, this paper introduced an adaptive multiscale framework that is based on the following idea. The reduction of discretization error by adaptive refinement may lead to a situation in which element size become comparable to the microstructure length-scale (or RVE size). In this condition, we showed that the solution induces a finite homogenization error that tends to increase as refinement proceeds. Based on this concept, we introduced an adaptive concurrent multiscale method in which below a certain size, continuum elements are replaced by explicit RVEs. In this context, we derived a set of bridging scale conditions,

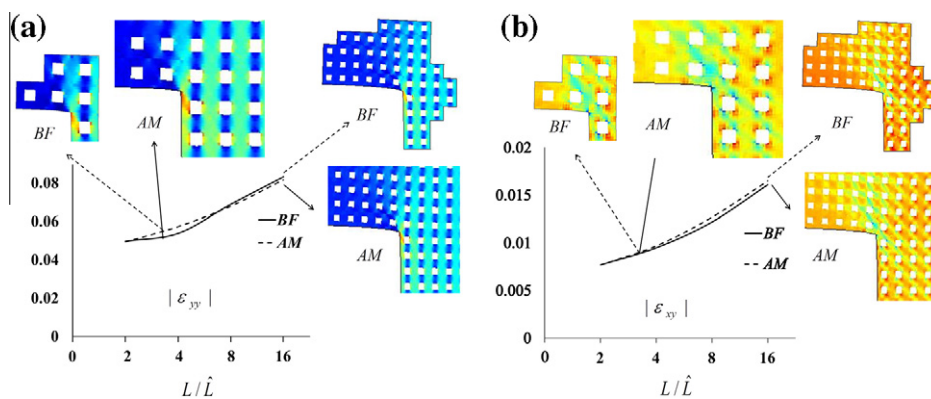


Fig. 14. Comparison between Brute Force approach (BF) and Adaptive Multiscale method (AM) accuracy for four different ratios of  $L/\hat{L}$  for (a) strain in Y direction and (b) shear strain.

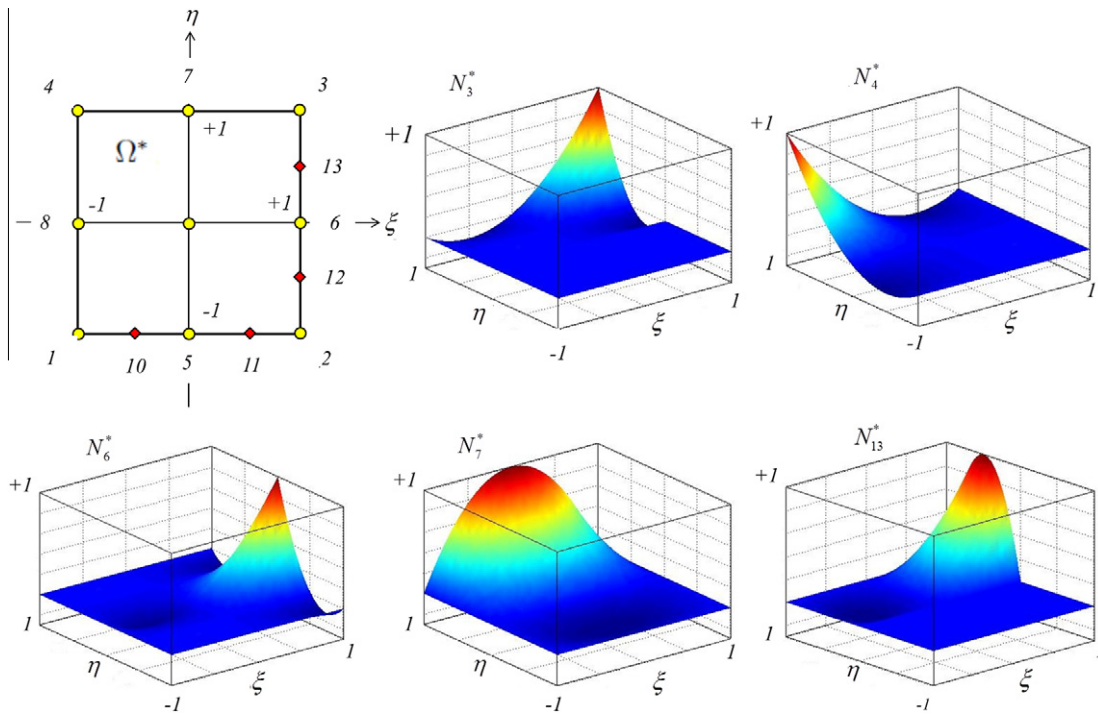


Fig. 16. An irregular element with four hanging nodes on two edges and associated shape functions.

consistent with traditional homogenization theory that naturally enable RVE to coexist with surrounding larger continuum elements. By adequately combining the concept of adaptive refinement and that of embedded RVEs, we then introduced a flexible concurrent multiscale framework in which one can obtain optimal macroscale and microscale accuracy with minimal computational cost.

Although the efficiency of the method was demonstrated with several examples, it still, at this point, suffers from few limitations. First, due to their inherent periodicity, RVEs must originally possess a rectangular shape, which in turn enforces that the macroscopic finite element mesh should be regular and rectangular. While this feature is usually not convenient when modeling domains that possess curved boundaries and internal interfaces, this limitation can be addressed by invoking flexible formulations that describe interfaces independent from discretization. An example of such a formulation is provided by the extended finite element method [33]. Second, the present work focussed on the case of small deformation, linear elastic problems, which is usually restrictive for most real-life applications. In fact, the proposed framework can naturally be extended to describe nonlinear material behaviors and finite strains, such as observed during plastic deformation, damage and fracture [44,27]. In particular, the adaptive multiscale method provides an ideal platform on which to study the phenomenon of ductile fracture, in which large scale features and local deformation mechanisms in the process zone must be modeled with maximum precision [46,45]. The potential of the method is therefore significant as it will, by enabling simulations of ductile fracture at multiple scales, relate macroscopic fracture toughness to the nature of a material's microstructures; this capability is crucial for the development of future high-toughness materials.

## Acknowledgements

The authors gratefully acknowledge National Science Foundation, for supporting this paper under NSF Grant No. CMMI-0900607 and CMMI 0927585 awards.

## Appendix A

### A.1. Element subdivision and shape functions

As depicted in Fig. 6, local mesh refinement causes the appearance of so-called “irregular nodes” (or “hanging nodes”) [15] on the boundaries between refined and unrefined domains. Subsequently, unrefined elements, which hold these types of nodes, are known as “irregular elements”. Two different approaches have been introduced in literature [15] in order to deal with this kind of irregularity:

- (1) *Constrained approximation*: In this method [1], no degrees of freedom are associated with *hanging nodes* and the stiffness matrix is assembled using the standard shape functions. However, since standard shape functions do not satisfy conformity of displacement on the element's boundaries, it is assumed that the displacement of such nodes is the average of two adjacent regular nodes. Therefore, a pair of constraints are applied on each *hanging node* to enforce that their displacement remains in between adjacent regular nodes. These constraints can be applied by means of the *Lagrange-Multipliers* method or by multiplying the global stiffness matrix by a so-called connectivity matrix.
- (2) *Conforming shape functions*: This method [22] consists of assembling the global stiffness matrix by introducing new shape functions, which satisfy both partition of unity and conformity of displacement on the edges of *irregular elements*.

Since in our method, the macro–micro bridging is accomplished by constraining micro nodes to macro nodes, for the ease of implementation, we adopted the second approach. We also restricted ourself to *1-irregular* mesh (the definition for which can be found in [15]). As shown in Fig. 15b, for the case of *1-irregular* mesh, the method permits the incorporation of two additional *hanging nodes* on each edge of 9-node quadrilateral *irregular element*. Sbaraj and Dokainsh [41] presented an approach to formulate new shape

functions for transition quadrilateral finite element for mesh grading. Following a similar approach, we introduced new sets of shape functions for 9-node quadrilateral elements. In what follows, shape functions are defined on quadrilateral 9-node parent element defined by  $\Omega^*$  (Fig. 15). In order to satisfy the conformity of displacement, shape functions associated with all possible hanging nodes, (Fig. 15b), for all  $\xi, \eta \in \Omega^*$ , can be written as:

$$\begin{aligned} N_{10}^* &= (-4\xi(1+\xi) \cdot H(-\xi)) \cdot (-0.5\eta(1-\eta)), \\ N_{11}^* &= (+4\xi(1-\xi) \cdot H(+\xi)) \cdot (-0.5\eta(1-\eta)), \\ N_{12}^* &= (+0.5\xi(1+\xi)) \cdot (-4\eta(1+\eta) \cdot H(-\eta)), \\ N_{13}^* &= (+0.5\xi(1+\xi)) \cdot (+4\eta(1-\eta) \cdot H(+\eta)), \\ N_{14}^* &= (+4\xi(1-\xi) \cdot H(+\xi)) \cdot (+0.5\eta(1+\eta)), \\ N_{15}^* &= (-4\xi(1+\xi) \cdot H(-\xi)) \cdot (+0.5\eta(1+\eta)), \\ N_{16}^* &= (-0.5\xi(1-\xi)) \cdot (+4\eta(1-\eta) \cdot H(+\eta)), \\ N_{17}^* &= (-0.5\xi(1-\xi)) \cdot (-4\eta(1+\eta) \cdot H(-\eta)). \end{aligned} \quad (37)$$

In this definition  $H$  is Heaviside function defined by:

$$H(\chi) = \begin{cases} +1 & \text{for } \chi > 0, \\ 0 & \text{for } \chi < 0 \end{cases} \quad (38)$$

Once an *irregular node*  $i$  ( $i = 10, 11, \dots, 17$ ) (Fig. 15b) exists, it takes the value  $N_i^*$  in (37), otherwise, it vanishes for all  $\xi, \eta \in \Omega^*$ . In addition, the standard quadratic shape functions,  $N_i$  ( $i = 1, 2, \dots, 9$ ), are modified as:

$$\begin{aligned} N_1^* &= N_1 - 0.375(N_{10}^* + N_{17}^*) + 0.125(N_{11}^* + N_{16}^*), \\ N_2^* &= N_2 - 0.375(N_{11}^* + N_{12}^*) + 0.125(N_{10}^* + N_{13}^*), \\ N_3^* &= N_3 - 0.375(N_{13}^* + N_{14}^*) + 0.125(N_{12}^* + N_{15}^*), \\ N_4^* &= N_4 - 0.375(N_{15}^* + N_{16}^*) + 0.125(N_{14}^* + N_{17}^*), \\ N_5^* &= N_5 - 0.75(N_{10}^* + N_{11}^*), \\ N_6^* &= N_6 - 0.75(N_{12}^* + N_{13}^*), \\ N_7^* &= N_7 - 0.75(N_{14}^* + N_{15}^*), \\ N_8^* &= N_8 - 0.75(N_{16}^* + N_{17}^*), \\ N_9^* &= N_9. \end{aligned} \quad (39)$$

This method satisfies both the partition of unity and conformity of displacement between adjacent elements. Fig. 16 shows an *irregular element* with four *hanging nodes*, and some of its shape functions.

## References

- [1] M. Ainsworth, B. Senior, Aspects of an adaptive hp-finite element method: adaptive strategy, conforming approximation and efficient solvers, *Comput. Methods Appl. Mech. Engrg.* 150 (1997) 65–87.
- [2] W.B. Anderson, R.S. Lakes, Size effects due to Cosserat elasticity and surface damage in closed-cell polymethacrylimide foam, *J. Mater. Sci.* 29 (1994) 6413–6419.
- [3] Z.P. Bazant, G. Pijaudier-Cabot, Nonlocal continuum damage, localization instability and convergence, *ASME J. Appl. Mech.* 57 (1988) 287–293.
- [4] Z.P. Bazant, M. Jirasek, Nonlocal integral formulations of plasticity and damage: survey of progress, *ASME J. Appl. Mech.* 128 (11) (2002) 1119–1149.
- [5] Z.P. Bazant, J. Ozbolt, Nonlocal microplane model for fracture, damage and size effect in structures, *ASME J. Appl. Mech.* 116 (11) (1990) 2484–2504.
- [6] T. Belytschko, S.P. Xiao, Coupling methods for continuum model with molecular model, *Int. J. Multiscale Engrg.* 1 (1) (2003) 115–126.
- [7] R. Borst, J. Pamin, R.H.J. Peerlings, L.J. Sluys, On gradient-enhanced damage and plasticity models for failure in quasi-brittle and frictional materials, *Comput. Mech.* 17 (1) (1995) 130–141.
- [8] E. Cosserat, F. Cosserat, *Theorie des corps deformables*, Hermann, Paris, 1909.
- [9] E.F. D'Azevedo, Optimal triangular mesh generation by coordinate transformation, *SIAM J. Sci. Comput.* 12 (4) (1991) 755–786.
- [10] R. de Borst, Simulation of strain localization: a reappraisal of the Cosserat continuum, *Engrg. Comput.* 8 (4) (1991) 317–332.
- [11] W.J. Drugan, J.R. Willis, A micromechanics-based nonlocal constitutive equation and estimates of representative volume element size for elastic composites, *J. Mech. Phys. Solids* 44 (4) (1996) 497–524.
- [12] N.A. Fleck, J.W. Hutchinson, A phenomenological theory for strain gradient effects in plasticity, *J. Mech. Phys. Solids* 41 (12) (1993) 1825–1857.
- [13] N.A. Fleck, G.M. Muller, M.F. Ashby, J.W. Hutchinson, Strain gradient plasticity: theory and experiment, *Acta Metall. Mater.* 42 (2) (1994) 475–487.
- [14] S. Forest, K. Sab, Cosserat overall modeling of heterogeneous materials, *Mech. Res. Commun.* 25 (4) (1998) 449–454.
- [15] T.P. Fries, A. Byfut, A. Alizada, K.W. Cheng, A. Schröder, Hanging nodes and xfem, *Int. J. Numer. Methods Engrg.* 86 (2011) 404–430.
- [16] S. Ghosh, J. Bai, P. Raghavan, Concurrent multi-level model for damage evolution in microstructurally debonding composites, *Mech. Mater.* 39 (2007) 241–266.
- [17] S. Ghosh, K. Lee, S. Moorthy, Multiple scale analysis of heterogeneous elastic structures using homogenisation theory and voronoi cell finite element method, *Int. J. Solids Struct.* 32 (1) (1995) 27–62.
- [18] S. Ghosh, K. Lee, S. Moorthy, Two scale analysis of heterogeneous elastic plastic materials with asymptotic homogenisation and voronoi cell finite element model, *Comput. Methods Appl. Mech. Engrg.* 132 (1996) 63–116.
- [19] S. Ghosh, K. Lee, P. Raghavan, A multi-level computational model for multi-scale damage analysis in composite and porous materials, *Int. J. Solids Struct.* 38 (2001) 2335–2385.
- [20] P.R. Guduru, A.J. Rosakis, G. Ravichandran, Dynamic shear bands: an investigation using high speed optical and infrared diagnostic, *Mech. Mater.* 33 (2001) 371–402.
- [21] J.M. Guedes, N. Kikuchi, Preprocessing and postprocessing for materials based on the homogenization method with adaptive finite element methods, *Comput. Methods Appl. Mech. Engrg.* 83 (2) (1990) 143–198.
- [22] A.K. Gupta, A finite element for transition from a fine grid to a coarse grid, *Int. J. Numer. Methods Engrg.* 12 (1978) 35–45.
- [23] M.E. Gurtin, A. Needleman, Boundary conditions in small-deformation, single-crystal plasticity that account for the burgers vector, *J. Mech. Phys. Solids* 53 (1) (2005) 1.
- [24] D. Guzman, M.S. Neubauer, G. Flinn, W.D. Nix, The role of indentation depth on the measured hardness of materials, *Mater. Res. Symp. Proc.* 308 (1993) 613–618.
- [25] R. Hill, Elastic properties of reinforced solids: some theoretical principles, *J. Mech. Phys. Solids* 11 (1963) 357–372.
- [26] Y. Huang, L. Zhang, T.F. Guo, K.C. Hwang, Mixed mode near-tip fields for cracks in materials with strain-gradient effects, *J. Mech. Phys. Solids* 45 (1997) 439–465.
- [27] F.J. Vernerey, C. McVeigh, W.K. Liu, B. Moran, D. Tewari, D. Parks, G. Olson, The 3d computational modeling of shear dominated ductile failure of steel, *JOM, J. Miner. Metals Mater. Soc.* (2006).
- [28] T. Kanit, S. Forest, I. Galliet, V. Mounoury, D. Jeulin, Determination of the size of the representative volume element for random composites: statistical and numerical approach, *Int. J. Solids Struct.* 40 (2003) 3647–3679.
- [29] V. Kouznetsova, W.A.M. Brekelmans, F.P.T. Baaijens, An approach to micromacro modelling of heterogeneous materials, *Comput. Mech.* 27 (2001) 37–48.
- [30] V. Kouznetsova, M.G.D. Geers, W.A.M. Brekelmans, Multi-scale constitutive modelling of heterogeneous materials with a gradient-enhanced computational homogenization scheme, *Int. J. Numer. Methods Engrg.* 54 (2002) 1235–1260.
- [31] W.K. Liu, E.G. Karpov, S. Zhang, H.S. Park, An introduction to computational nanomechanics and materials, *Comput. Methods Appl. Mech. Engrg.* 193 (2004) 1529–1578.
- [32] Q. Ma, D.R. Clarke, Size dependent hardness in silver single crystals, *J. Mater. Res.* 10 (1995) 853–863.
- [33] S. Mohammadi, Extended finite element method: for fracture analysis of structures, Blackwell Publishing Ltd., Oxford, 2008.
- [34] S. Moorthy, S. Ghosh, A model for analysis of arbitrary composite and porous microstructures with voronoi cell finite elements, *Int. J. Numer. Methods Engrg.* 39 (1996) 2363–2398.
- [35] J.W. Hutchinson, M.R. Begley, The mechanics of size-dependent indentation, *J. Mech. Phys. Solids* 4 (10) (1998) 2049–2068.
- [36] S. Nemat-Nasser, M. Hori, *Micromechanics: Overall Properties of Heterogeneous Materials*, Elsevier, Amsterdam, 1993.
- [37] H.S. Park, W.K. Liu, An introduction and tutorial on multiple-scale analysis in solids, *Comput. Methods Appl. Mech. Engrg.* 193 (2004) 201–217.
- [38] P. Raghavan, S. Ghosh, Adaptive multi-scale computational modeling of composite materials, *Science* 5 (2) (2004) 151–170.
- [39] P. Raghavan, S. Ghosh, Concurrent multi-scale analysis of elastic composites by a multi-level computational model, *Mech. Mater.* 193 (2007) 497–538.
- [40] Sh.I. Ranganathan, M. Ostojic-Starzewski, Scaling function, anisotropy and the size of rve in elastic random polycrystals, *J. Mech. Phys. Solids* 53 (2008) 2773–2791.
- [41] K. Subbaraj, M.A. Dokainish, Side-node transition quadrilateral finite elements for mesh-grading, *Comput. Struct.* 30 (5) (1988) 117–118.
- [42] P.M. Suquet, Local and global aspects in the mathematical theory of plasticity, Elsevier Applied Science Publishers, London, 1985.
- [43] F.J. Vernerey, M. Farsad, An eulerian/xfem formulation for the large deformation of cortical cell membrane, *Comput. Methods Biomech. Biomed. Engrg.* 14 (5) (2011) 433–445.
- [44] F.J. Vernerey, W.K. Liu, B. Moran, Multi-scale micromorphic theory for hierarchical materials, *J. Mech. Phys. Solids* 55 (12) (2007) 2603–2651.
- [45] F.J. Vernerey, W.K. Liu, B. Moran, G.B. Olson, A micromorphic model for the multiple scale failure of heterogeneous materials, *J. Mech. Phys. Solids* 56 (4) (2008) 1320–1347.
- [46] F.J. Vernerey, W.K. Liu, B. Moran, G.B. Olson, Multi-length scale micromorphic process zone model, *Comput. Mech.* 44 (2009) 433–445.

- [47] F.J. Vernerey, F. Barthelat, On the mechanics of fish-scale structures, *Int. J. Solids Struct.* 47 (17) (2010) 2268–2275.
- [48] F.J. Vernerey, M. Farsad, A constrained mixture approach to mechano-sensing and force generation in contractile cell, *J. Mech. Behavior Biomed. Mater.* 4 (8) (2001) 1683–1699.
- [49] F.J. Vernerey, L. Foucard, M. Farsad, Bridging the scales to explore cellular adaptation and remodeling, *BionanoScience* 1 (3) (2011) 110–115.
- [50] G.J. Wagner, W.K. Liu, Coupling of atomistic and continuum simulations using a bridging scale decomposition, *Comput. Mater. Sci.* 190 (2003) 249–274.
- [51] A.A. Yazdani, A. Gakwaya, G. Dhatt, A posteriori error estimator based on the second derivative of the displacement field for two-dimensional elastic problems, *Comput. Struct.* 62 (2) (1997) 317–338.
- [52] A.M. Gokhale, Z. Shan, Representative volume element for non-uniform microstructure, *Comput. Mater. Sci.* 24 (2002) 361–379.
- [53] D. Zhu, C. Ortega, R. Motamedi, L. Szewciw, F.J. Vernerey, F. Barthelat, Structure and mechanical performance of a “modern” fish scale, *Adv. Biomater.*, <http://dx.doi.org/10.1002/adem.201180057>.
- [54] T.I. Zohdi, J.T. Oden, G.J. Rodin, Hierarchical modeling of heterogeneous bodies, *Comput. Methods Appl. Mech. Engrg.* 138 (1996) 273–298.